2D Semi-metallic Hafnium Ditelluride: A Novel Nonlinear Optical Material for Ultrafast and Ultranarrow Photonics Applications

Safayet Ahmed[1,3,†], Yiyu Gan[2,†], Ahmed Mortuza Saleque [1,3], Honglei Wu[2], Junpeng Qiao[4], Md. Nahian Al Subri Ivan[1,3], Sumaiya Umme Hani[1,3], Tawsif Ibne Alam[1,3], Qiao Wen[2*] and Yuen Hong Tsang[1,3*]

[1]*Department of Applied Physics, Materials Research Center, Photonics Research Institute, and Research Institute for Advanced Manufacturing, The Hong Kong Polytechnic University, Hung Hom, Kowloon, Hong Kong, China*

[2]*Key Laboratory of Optoelectronic Devices and Systems of Ministry of Education and Guangdong Province, College of Physics and Optoelectronic Engineering, Shenzhen University, Shenzhen 518060, China.*

[3]*Shenzhen Research Institute, The Hong Kong Polytechnic University, 518057 Shenzhen, Guangdong, China*

[4]*School of Physics and Physical Engineering, Qufu Normal University, Qufu 273165, China*

†S.Ahmed and Y. Gan contributed equally in this paper.

* Corresponding Authors

Corresponding Authors' mail: *yuen.tsang@polyu.edu.hk; wenqiao@szu.edu.cn*

Abstract

2D semi-metallic hafnium ditelluride ($HfTe_2$) material is used in several applications like solar steam generation, gas sensing, and catalysis owing to its strong near-infrared absorbance, high sensitivity, and distinctive electronic structure. The zero-bandgap characteristics, along with the thermal and dynamic stability of 2D-$HfTe_2$, make it a desirable choice for developing long-wavelength-range photonics devices. Herein, the $HfTe_2$-nanosheets are prepared using the liquid-phase exfoliation method, and their superior nonlinear optical properties are demonstrated by the obtained modulation depth of 11.9 % (800 nm) and 6.35% (1560 nm), respectively. Additionally, the observed transition from saturable to reverse saturable absorption indicates the adaptability of the prepared material in nonlinear optics. By utilizing a side polished fiber-based $HfTe_2$-saturable absorber (SA) inside an Er-doped fiber laser cavity, a mode-locked laser with 724 fs pulse width and 56.63 dB signal-to-noise ratio (SNR) is realized for the first time. The generated mode-locked laser with this SA has the second-lowest mode-locking threshold (18.35 mW) among the other 2D material-based SAs, paving the way for future laser development with improved

efficiency and reduced thermal impact. Finally, employing this $HfTe_2$-SA, a highly stable single-frequency fiber laser (SNR ~ 74.56 dB; Linewidth ~ 1.268 kHz) is generated for the first time, indicating its promising ultranarrow photonic application.

KEYWORDS: $HfTe_2$; 2D materials; Nonlinear Optics; Mode-locked laser; Single-frequency fiber laser.

1. Introduction

Since the discovery of graphene in 2004, ultra-thin 2D nanomaterials, for instance, graphene's elemental analogues (silicon, germanene, and phosphorene), transition metal dichalcogenides (TMDs), topological insulators (TIs), metal hydroxides/oxides, black phosphorus (BP), and boron nitrides, have attracted significant research interest from scientists due to their unique optical, chemical, and physical properties. [1–4] These 2D materials are used in various applications in catalysis, electronics, optoelectronics, and sensing platforms. The excellent contribution of 2D materials in nonlinear optical (NLO) research motivated scientists to explore more new materials in this field.[5–7] Recently, 2D semi-metallic TMDs like WTe_2 and $MoTe_2$ have been used in ultrafast nonlinear photonics due to their fast photocarrier dynamic and excellent NLO properties.[8,9] These materials' distinctive band structures and photo-excitations make them ideally suited for mid-infrared photonic applications. Among the other semi-metallic TMDs material, hafnium ditelluride ($HfTe_2$) is getting attention due to its significant application in medical sterilization, gas sensor, and superconductor.[10–12]

2D-$HfTe_2$, a semi-metallic compound belonging to the VIB group of transition metal dichalcogenides (TMDs),[13] has garnered little attention in the field of nonlinear optics and photonics, despite the fact that other materials in this group, such as HfS_2[14] and $HfSe_2$,[15] have been extensively studied for their effectiveness as saturable absorbers (SAs) in the generation of ultrafast lasers. The majority of work on $HfTe_2$ to date has

largely focused on its basic characteristics, such as its structure and stoichiometry,[16] theoretical and experimental electronic band structure,[17] electric transport properties,[18] and doping-affected band structure.[19] Due to its unique zero-bandgap structure,[19] semi-metallic $HfTe_2$ can absorb light over a wide range of wavelengths, making it suitable for photonics applications in the near to far-infrared regions of the electromagnetic spectrum.[20,21] Moreover, the higher dynamical and thermal stability[11] of the 2D-$HfTe_2$ make it ideal for developing different practical devices. Therefore, a thorough study of the 2D-$HfTe_2$ material's NLO characteristics and photonics applications is essential for developing the research field.

This contribution explores the NLO properties of multi-layered $HfTe_2$ nanosheets and their capability to develop ultrafast and ultranarrow photonic devices. Initially, $HfTe_2$-nanosheets were prepared by the liquid-phase exfoliation (LPE) method, and extensive material characterizations were performed to analyze the material composition, thickness, and absorption spectrum. Then by utilizing the density function theory (DFT), the electronic band structure of monolayer, bi-layer, and bulk $HfTe_2$ was realized. The NLO properties (nonlinear absorption, modulation depth, and nonlinear refractive index) of $HfTe_2$-nanosheets were determined using both open and closed-aperture Z-scan technology. The measure modulation depth of 11.9 % (800 nm) and 6.35% (1560 nm), respectively, indicated the excellent nonlinear optical characteristics of the prepared nanosheets. By dropping the nanosheet solution over the side polished fiber (SPF), SPF-based SA was prepared. Then by incorporating this $HfTe_2$-SA with an Er-doped fiber laser cavity, for the first time, a mode-locked pulsed laser with 724 fs pulse width was generated at the second smallest threshold pump power ever recorded (18.35 mW). This low-threshold pulsed laser will be incredibly helpful in the future development of laser sources with improved conversion efficiency and lower

thermal effects, which have great applications in material engineering, micro-machining, and medical imaging. Additionally, using this $HfTe_2$-SA, a single-frequency fiber laser (SFFL) is developed for the first time, with narrow linewidth and high signal-to-noise ratio (SNR) of 1.268 kHz and 74.56 dB, respectively. This SFFL will apply substantially in optical sensing, measurement, and coherent optical communication.[22,23] These results indicate that $HfTe_2$ is a superior nonlinear optical material for developing future photonic devices.

2. Results and Discussions

2.1 Material characterization of $HfTe_2$ nanosheets

In Fig. 1 (a), the scanning electron microscope (SEM) image of the prepared $HfTe_2$ nanosheets is shown, indicating the higher concentration of the prepared sample, which is suitable for the SA preparation. The main sample preparation steps are provided in the experimental section. To analyze the sample composition and purity of the samples, energy-dispersive X-ray spectroscopy (EDS) was performed with a relatively larger flake (Fig. 1b, top left) as it allows us to get the result more efficiently using the existing system. From the obtained result shown in Fig. 1b (top right), the purity of the sample can be confirmed as the sample contain Hf and Te with an atomic ratio of 1:2. In addition, the element mapping was also performed to check the distribution of the Hf and Te in the corresponding flake shown in Fig. 1b (bottom). The Raman spectrum of the bulk and nanosheets is demonstrated in Fig. 1 (c), which illustrates the peak at 120.37 cm^{-1} (nanosheets) and 118.44 cm^{-1} (bulk) corresponds to the E_g mode of $HfTe_2$.[13] Due to the size decrement, the Raman peak of the nanosheets experienced a redshift, which is similar to the other nanosheet results.[24] The thickness of the prepared nanosheets is analyzed using atomic force microscopy (AFM), as shown in Fig. 1(d). Three random lines are drawn to investigate the

thickness of the randomly selected nanosheet flakes. As illustrated in Fig. 1(e), the thickness of the nanosheets is nearly 65-75 nm, which confirms their 2D nanosheet characteristics. In addition, the distribution of thickness and lateral dimension along the short and long axis of the 537 nanosheet samples are analyzed as shown in Fig. S1 (Supporting Information). The average thickness of the prepared samples is measured at around 64.407 nm, whereas the average size in the long and short axis is realized as 0.52 µm and 1.2 µm, respectively. The X-ray diffraction (XRD) pattern was analyzed to check the crystalline planes of the prepared samples, as shown in Fig. 1(f). The XRD can define the polycrystalline nature of the prepared samples. The crystalline planes also match the previously reported JCPDS card No. 26-0736.[13] X-ray photoelectron spectroscopy (XPS) was performed to validate the stoichiometry of the prepared nanosheets. The XPS spectra of the $HfTe_2$ bulk and nanosheets are shown in Fig. 1 (g), which can distinguish the shift in surface chemical composition during the exfoliation process. The position of the peaks before and after the exfoliation remains consistent, proving the stable chemical state of the prepared nanosheet samples. Fig. S2(Supporting Information) shows the high-resolution XPS spectra of Hf 4f and T 3d. The XPS result is compatible with the previously reported result for $HfTe_2$ material. [13] For characterizing the material at the atomic level, the high-resolution TEM (HRTEM) and selected area electron diffraction (SAED) pattern was realized, as shown in Fig. 1(h). The crystalline of (100), (101), and (111) are defined in both the HRTEM image and SAED pattern, corresponding to the lattice spacing of 0.346 nm, 0.321 nm, and 0.195 nm, respectively. All these material characterizations indicate that the prepared samples are defect-free and belong to pristine 2D $HfTe_2$-nanosheets. The UV-Vis-NIR spectrum was realized to check the absorption of the prepared nanosheets covering the wavelength from 450 to 2000 nm.

The result indicates that $HfTe_2$ nanosheets have a broad absorption, which is favorable for various possible infrared optoelectronic device applications.[25,26]

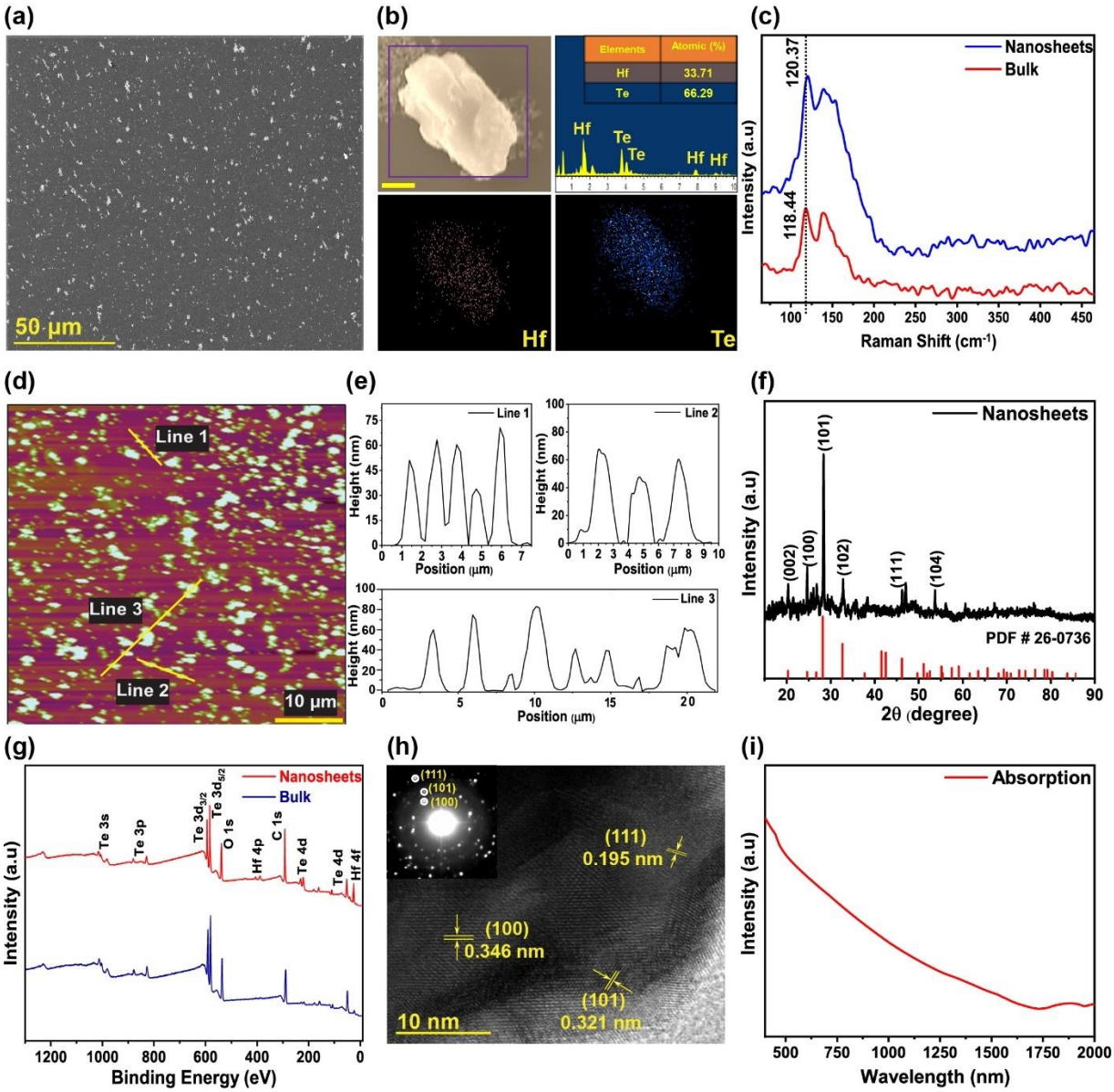

Figure 1. (a) SEM image of the exfoliated samples. (b) SEM image (top-left, scale is 2 μm and blue rectangle box defines the EDS area), EDS profile (top-right; inset is the atomic ratio of individual elements), and element mapping (Hf-bottom left; Te-bottom right) of a large $HfTe_2$-nanosheet flake. (c) Raman spectra of exfoliated nanosheets and bulk samples. (d) AFM image showing three lines. (e) The height profiles of the corresponding lines are shown in (d). (f) XRD peaks of the exfoliated nanosheets, along with the peaks obtained from standard JCPDS card No. 26-0736. (g) XPS-analysis of $HfTe_2$-bulk and nanosheets. (h) HRTEM image shows three planes of (100), (101), and (111); the inset shows the corresponding selected area diffraction (SAED) pattern. (i) UV-Vis-NIR spectrum of the exfoliated nanosheets.

2.2 Crystal Structure and Density function theory (DFT) calculation

The crystal structures (side view) of the monolayer, bi-layer, and bulk $HfTe_2$ are provided in Fig. 2 (a) – (c). $HfTe_2$ crystal exhibits a stable 1T-phase layered structure having a weak interlayer interaction. The crystal structure has been identified as a CaI_2 type of triangular arrangement and belongs to the *P*-3*m*1 space group. As observed from the crystal structures, Hf atoms are positioned between alternating layers of Te atoms with reverse symmetry at the top and bottom. The unit cell of $HfTe_2$ (Fig. S3, Supporting Information) is characterized by the distribution of Hf atoms at eight different apex angles and Te atoms arranged in a regular trigonal column, which is comprised of three lower and upper Hf atoms positioned at the center of the lower and upper halves respectively.

For analyzing the bandgap of the different layers of $HfTe_2$, density functional theory (DFT) was adopted. According to the Vienna ab initio simulation software (VASP, University of Vienna), all calculations were carried out using the projector-augmented plane-wave approach within the context of density functional theory (DFT).[27] For the exchange-correlation potential, Perdew-Burke-(PBE) Ernzerhof's generalized gradient approximation was implemented.[28] 500 eV was chosen as the plane wave cut-off energy. The Kohn-Sham equation was iteratively solved with the energy criterion of 10^{-5} eV. All structures were relaxed until the remaining forces on the atoms dropped to less than 0.02 eV/Å. The computed band structures of the monolayer, bi-layer, and bulk $HfTe_2$ are provided in Fig. 2 (d)-(f). For all the layers, no bandgap was recorded. It indicates that 2D- HfTe2 is a zero-bandgap based semimetal, and the bandgap does not vary with the layer number. Due to the zero bandgap, HfTe2 material can exhibit higher electron mobility, great optical transparency, and high thermal conductivity, making the material desirable for different photonic devices. Moreover, the lack of

bandgap allows the material to be used in wide range of wavelengths like near-infrared to far-infrared which is desirable for different photonics devices like saturable absorber, optical modulators, photodetectors, and light-emitting diodes.[29,30]

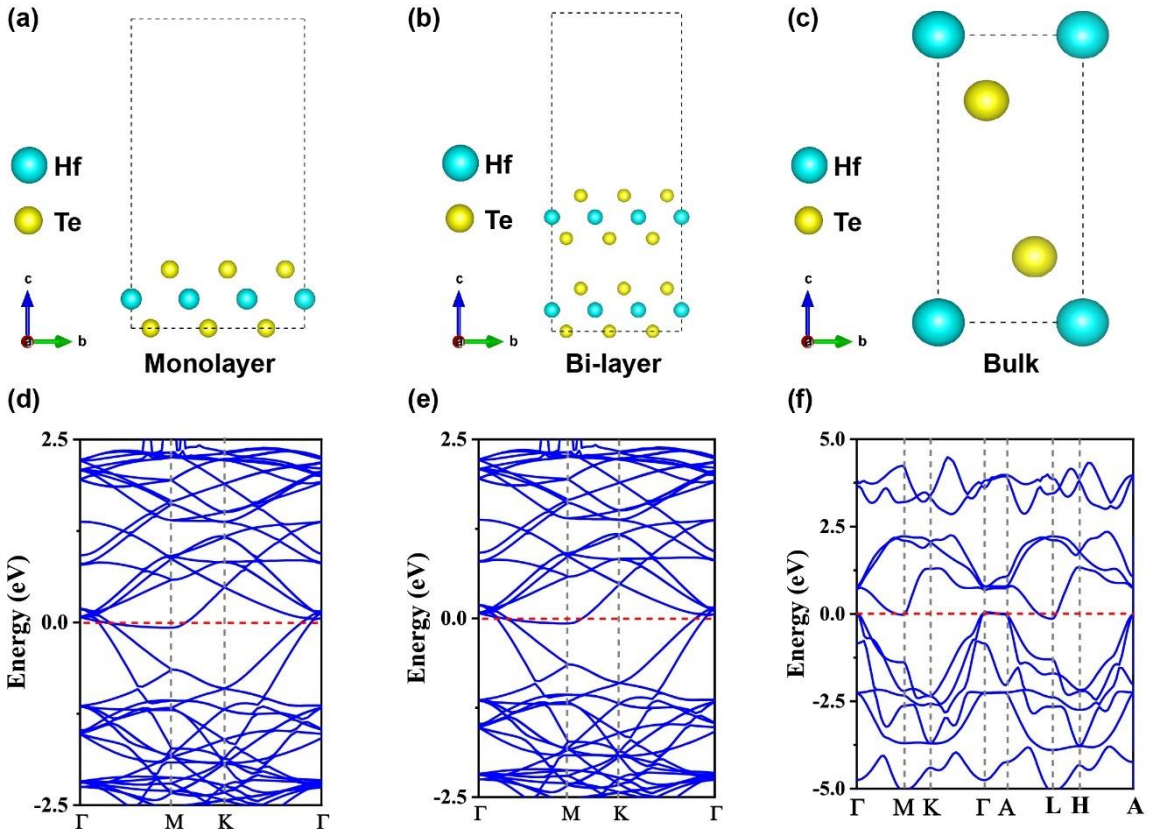

Figure 2. Side-view of the (a) monolayer, (b) bi-layer, and (c) bulk $HfTe_2$. Electronic band structures of the (a) monolayer, (b) bi-layer, and (c) bulk $HfTe_2$.

2.3 Nonlinear optical responses of $HfTe_2$ nanosheets

The open and closed aperture Z-scan technique was used to investigate the nonlinear optical responses of the prepared HfTe2-nanosheet. $HfTe_2$-IPA liquid solution was used as the sample by putting it inside a 1 mm quartz cuvette. The schematic of the Z-scan system is provided in Fig. S4a (Supporting Information). The experimental section provides all the descriptions regarding the laser configuration for this analysis. Several nonlinear absorption behaviors like saturable absorption, reverse saturable absorption, ground-state bleaching, and multiphoton absorption (MPA) can be observed when the samples are excited with a high-power laser.[31] Figures 3 (a), (c),

and (e) depict the open aperture (OA) findings for the respective sample for wavelengths of 800 nm and 1560 nm with varied intensities, respectively. The fitting of the OA results was made by equation 1 [31] based on the nonlinear beam propagation model. From the fitting results, nonlinear absorption coefficients (*β*) were determined.

$$T(z) = \sum_{n=0}^{\infty} \frac{\left(-\beta I_0 L_{eff}\right)^n}{\left(1+{z^2}/{z_0^2}\right)^n (n+1)^{3/2}} \approx 1 - \frac{\beta I_0 L_{eff}}{2^{3/2}\left(1+{z^2}/{z_0^2}\right)} \quad (1)$$

where $T(z)$ represents the normalized transmittance, z is the position of the sample, z_0 is the Rayleigh length, I_0 is the peak intensity at the focus, and L_{eff} is the effective length. All the associated equations regarding equation 1 are given in the supporting information notes (NS2).

The saturable absorption property of the prepared samples can be observed from the 800 nm OA results (Fig.3a), where the transmittance rises as the sample moves from –Z to +Z for both of the laser intensities (0.836 and 1.37 MW/cm^2, respectively). The measured *β* value is negative for these cases (-1.75 ×10^3 cm/GW and -3.51×10^3 cm/GW). No reverse saturable absorption (RSA) phenomenon is observed for this excited laser wavelength. From Fig. 3 (c) and (e), the OA results for the 1560 nm wavelength are shown. For the lower intensities (36.18, 50.11, and 64.57 MW/cm^2), the sample showed saturable absorption property as the transmittance increased as the sample moved towards the focusing point (Z = 0). The *β* values for the saturable absorption cases at 1560 nm varied from -70 to -36 cm/GW, as shown in Fig. 3(f). The Pauli blocking principle can be used to explain saturable absorption. According to this theory, it is impossible to excite electrons in a solid substance to higher energy levels if such levels are already occupied. High-intensity light increases the occupation of the energy levels in the event of saturable absorption, decreasing the number of levels that are accessible for additional excitation. As a result, the phenomenon of saturable

absorption results in a decrease in light absorption as light intensity increases. High-intensity light can pass through the material due to the reduction in absorption.[32]

As the intensity of the laser increased to 78.97 and 93.58 MW/cm^2, respectively, the sample demonstrated RSA property, therefore, the transmittance decreased as the sample moved towards the focus point (Fig. 3e). The measured β values are positive (91 and 141 cm/GW) for RSA. in RSA phenomenon, with the increase of the optical intensity, the absorption coefficient also increases, resulting in the reduction of optical transmission of the sample. The excited state absorption process is typically attributed to the transition from saturable absorption to RSA. [33] All the OA results indicate that the β value significantly depends on the laser intensity as reported for 2D materials. [31,34] The third-order nonlinear optical susceptibility (Im χ^3) is related to the β value significantly, whereas the figure of merit (FOM) for the third-order optical nonlinearity is correlated to Im χ^3. All of these values are measured and listed in Table 1. The related equation for calculating these parameters is provided in the supporting information notes (NS2). By using the conventional one-photon absorption model (equation 2),[35] the normalized transmittance versus input intensity of $HfTe_2$-nanosheets are realized as given in Fig. 3 (b), (d) and Fig. S4 (Supporting Information) for two different wavelengths of 800 nm and 1560 nm with varied intensities.

$$T = 1 - \frac{\alpha_s}{1+{}^{I_0}/_{I_{sat}}} + \alpha_{ns} \quad (2)$$

where I_0 is the intensity of the incident light, I_{sat} is the saturable intensity, α_s is the modulation depth, and α_{ns} is the non-saturable loss.[59,60] The largest values of α_s were measured as 11.5% and 6.35% for wavelengths of 800 nm and 1560 nm, respectively. Moreover, the calculated lower value of I_{sat} (4.95 MW/cm^2) at 1560 nm is beneficial for generating mode-locked laser pulses at a lower threshold, facilitating the designing of self-mode-locked laser sources with higher efficiency and lower thermal impact. All

these nonlinear characterizations of $HfTe_2$-nanosheets indicate that this material has excellent saturable absorption properties, leading to the fabrication of effective $HfTe_2$-based saturable absorbers for ultrafast laser generation, as described in the following section.

The CA Z-scan results were determined by using a 1560 nm laser source at an intensity of 36.16 MW/cm^2, as shown in Fig. S5 (Supporting Information). The obtained experimental results are fitted by applying equation 3, where $\Delta\Phi$ is the nonlinear phase shift value. [36] By using the equation 4, the value of $\Delta\Phi$ can be determined, where I_0 is the peak intensity at the focus, n_2 is the nonlinear refractive index, λ_c is the central wavelength, and L_{eff} is the effective length. Additionally, the nonlinear refraction response without the nonlinear absorption effect was calculated by measuring the value of n_2 using CA/OA Z-scan results. The value of n_2 of the $HfTe_2$ sample was determined as -6.3 cm^2/GW.

$$T(z) = \frac{1}{1-\frac{4z/z_0}{\left(1+z^2/z_0^2\right)^2}\Delta\Phi+\frac{4}{\left(1+z^2/z_0^2\right)^3}\Delta\Phi^2} \quad (3)$$

$$\Delta\Phi = 2\pi n_2 I_0 L_{eff}/\lambda_c \quad (4)$$

Additionally, since the $HfTe_2$-IPA sample combination was employed in the Z-scan method, we conducted an OA test using just IPA within the cuvette to validate that all the findings are attributable to the $HfTe_2$ material and not from IPA, as shown in Fig. S6 (Supporting Information). The fact that there was no apparent increase in transmittance at the IPA focusing point shows that all data were obtained using $HfTe_2$-nanosheets.

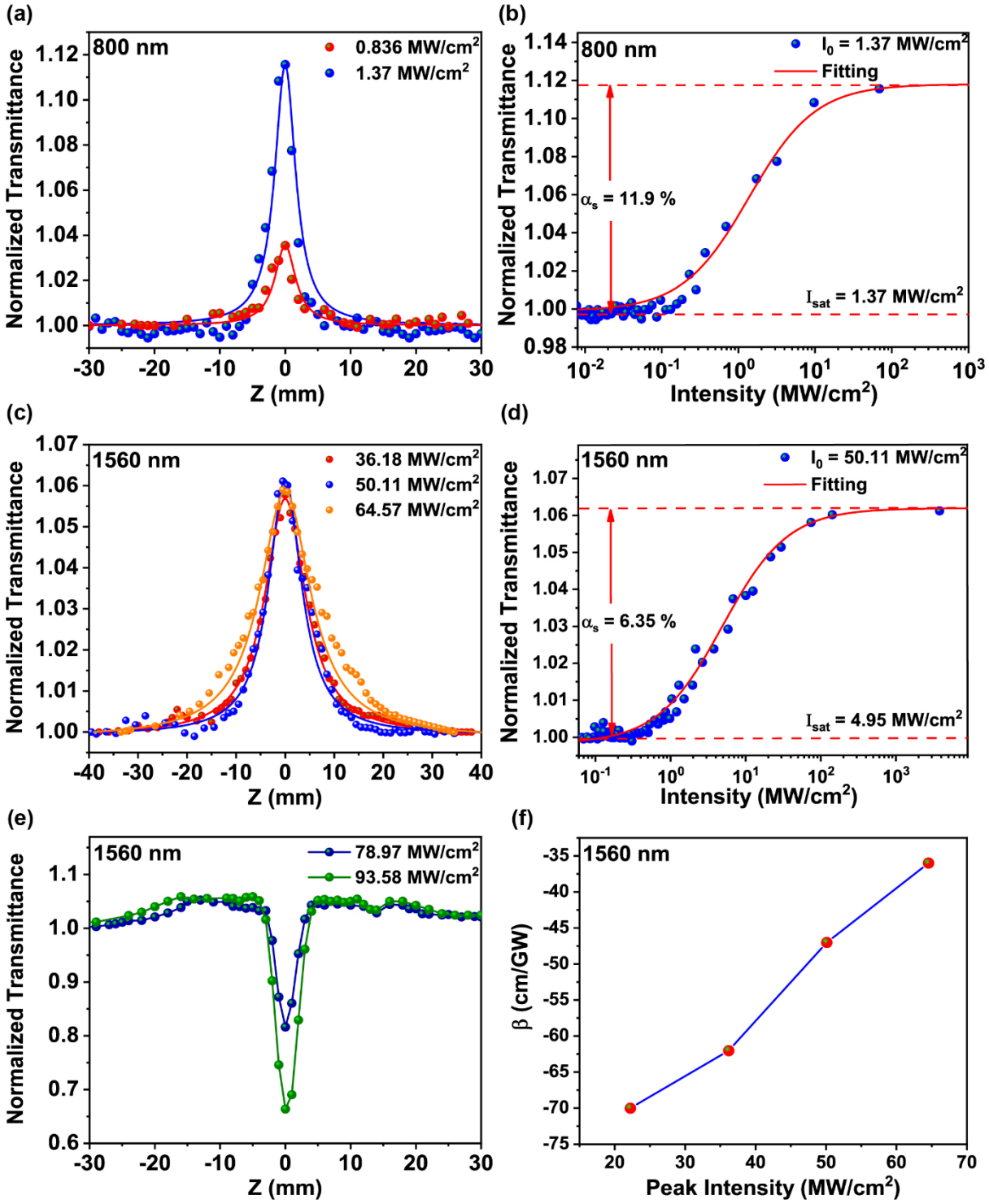

Figure 3. Nonlinear optical absorption response in HfTe2-IPA sample. Open aperture Z-scan measurement of the HfTe2-nanosheets at the wavelength of (a) 800nm and (c) 1560 nm. Here, the dots represent the findings of the experiment, while the accompanying solid lines of the same color represent the fitting results. Normalized transmittance vs the intensities at (b) 800nm, (d) 1560 nm (lower intensity), and (e) 1560 nm (higher intensity). (f) The change of nonlinear absorption coefficient (β) for peak intensity at 1560 nm for saturable absorption. α_s: Modulation depth; I_{sat}: saturation intensity.

Table 1 Nonlinear optical parameters of $HfTe_2$ nanosheets at two wavelengths using the OA Z-scan method. α_s: modulation Depth; β: nonlinear absorption coefficient; I_{sat}: saturable intensity; Im χ^3: imaginary part of the third-order nonlinear optical susceptibility; FOM: figure of meri; RSA: reverse saturable absorption.

λ (nm)	Peak Intensity (MW cm^{-2})	α_s(%)	I_{sat} (MW cm^{-2})	β (cm GW^{-2})	Im χ^3 (× 10^{-9} esu)	FOM (× 10^{-12} esu)
800	0.836	3.8	0.67	-1.75×10^3	-0.46	-105
	1.37	11.9	1.37	-3.51×10^3	-1.70	-204
1566	36.16	-	-	-62	-0.0585	-8.71
	50.11	6.35	4.95	-47	-0.044	-7.19
	64.57	6.15	3.05	-36	-0.034	-5.16
	78.97	-	-	91 (RSA)	-0.0859	12.9
	93.58	-	-	141 (RSA)	-0.133	20.1

2.4 Ultrafast and Ultranarrow Photonics Applications of $HfTe_2$ nanosheets

After analyzing the NLO properties of prepared $HfTe_2$-nanosheets, an SPF-based $HfTe_2$-SA is prepared by drop casting the liquid solution over an SPF and dried at room temperature. In comparison to other forms of SAs, SPF-based SAs provide several benefits. First, more effective saturable absorption is made possible by the interaction of the intracavity beam's evanescent field with the material on the side of the fiber. Second, the SA material's deposition length can be precisely tuned to the fiber's characteristics, improving output performance. Third, because the interacting radiation has a low intensity, SPFs have a relatively high damage threshold. As a result, SPF-based SAs are a preferable option for the development of high-power or high-repetition-rate pulse-based laser sources. Then the $HfTe_2$-SA is connected to an Erbium-doped fiber ring cavity after analyzing its application for SFFL generation. The Information regarding the fibers used in the cavity, along with the group velocity and net cavity dispersion, is provided in the supporting information note (NS3)**.** As shown

in Fig. 4 (a), the ring cavity consists of a 976 nm laser pump diode connected with the gain medium (erbium-doped fiber) through a 980/1550 nm wavelength division multiplexer (WDM). A polarization independent-isolator (PI-ISO) has been incorporated to ensure unidirectional light flow within the cavity. Fine-tuning of the intracavity birefringence and polarization state is achieved using a three-paddle polarization controller (PC). The SPF-based $HfTe_2$-SA is then connected to the cavity to modulate light absorption with intensity, thus enabling the generation of ultrashort pulses through the mode-locking operation. Finally, an output coupler (OC) is utilized to take the output to the specific equipment for analyzing the result and completing the ring cavity. A detailed description of the equipment used can be found in the experimental section.

In this ring cavity, a stable mode-locking operation was achieved when the pump power was at 18.35 mW. The recorded power is the second lower threshold power ever recorded for a mode-locking operation using 2D material-based SAs. The obtained mode-locking threshold was approximately 170% lower compared to the other Hf-based SAs.[14,15] Due to the excellent nonlinear optical properties of $HfTe_2$, it is possible to get the mode-locking operation in such a low threshold pump power. The low-threshold mode-locking allows for a laser to be operated at lower overall power, reducing the potential for heat damage to the laser's components and permitting the design of self-starting mode-locking operations essential for high-speed communication, spectroscopy, and material processing. The recorded pulse-pulse repetition interval of the generated mode-locked pulse is 127.4 ns, as shown in Fig. 4 (b), corresponding with the cavity length of 26.3m, confirming the mode-locked pulse generation. The inset of Fig. 4 (b) demonstrates the original oscilloscope image of the long-range pulse train at 10 μs/div, which confirms the high stability of the generated

pulses. The central wavelength of 1557.94 nm and the 3-dB bandwidth of 3.557 nm are recorded from the wave spectrum, as shown in Fig. 4 (c). The Kelly sidebands of the spectrum indicate the generation of a soliton mode-locked laser. The development of the optical spectra of the solution pulses over 5 hours is depicted in Fig. S7 (Supporting Information), demonstrating the high stability of the generated Er-doped mode-locked fiber laser. The radio-frequency spectrum (Fig. 4d) also defines the fundamental repetition rate of 7.86 MHz with 56.63 dB signal-to-noise ratio (SNR). The high SNR and the long-range RF spectrum (inset of Fig. 4d) illustrate the stability of the generated laser. From the autocorrelator trace of the generated laser, the pulse width is realized as 724 fs (fitted with $sech^2$ profile). The time-bandwidth product (TBP) was calculated as 0.318 based on the 3-dB bandwidth of the wave spectrum and the pulse width, which is slightly higher than the theoretical transformation limit value of 0.315, indicating a little chirping of the mode-locked pulses.[26] Finally, the average output power of the generated pulses is determined with respect to the pump power, as shown in Fig. 4 (f). The average output power increased from 0.389 mW to 2.51 mW with a slope efficiency of 2.77 %, demonstrating a good linear correlation between input and output power. The maximum peak power and single pulse energy are determined to be 388.15 W and 0.319 nJ, respectively, considering the maximum output powers, pulse durations, and pulse repetition rates. These values are critical for various functional applications, including mechanical machining, medical surgery, spectroscopes, and chemical reactions. A comparison table of different 2D material based SAs for ultrafast generation is presented in Table 2. The table shows that the threshold of the mode-locked pulse obtained with $HfTe_2$-SA is the second lowest after $NbSe_2$-QDs SA. However, the pulse width is narrower for $HfTe_2$-SA compared to $NbSe_2$-QDs SA. Additionally, compared to other 2D materials like graphene,

topological insulators, and other TMDs, HfTe2-SA has shown comparable results in ultrafast laser generation.

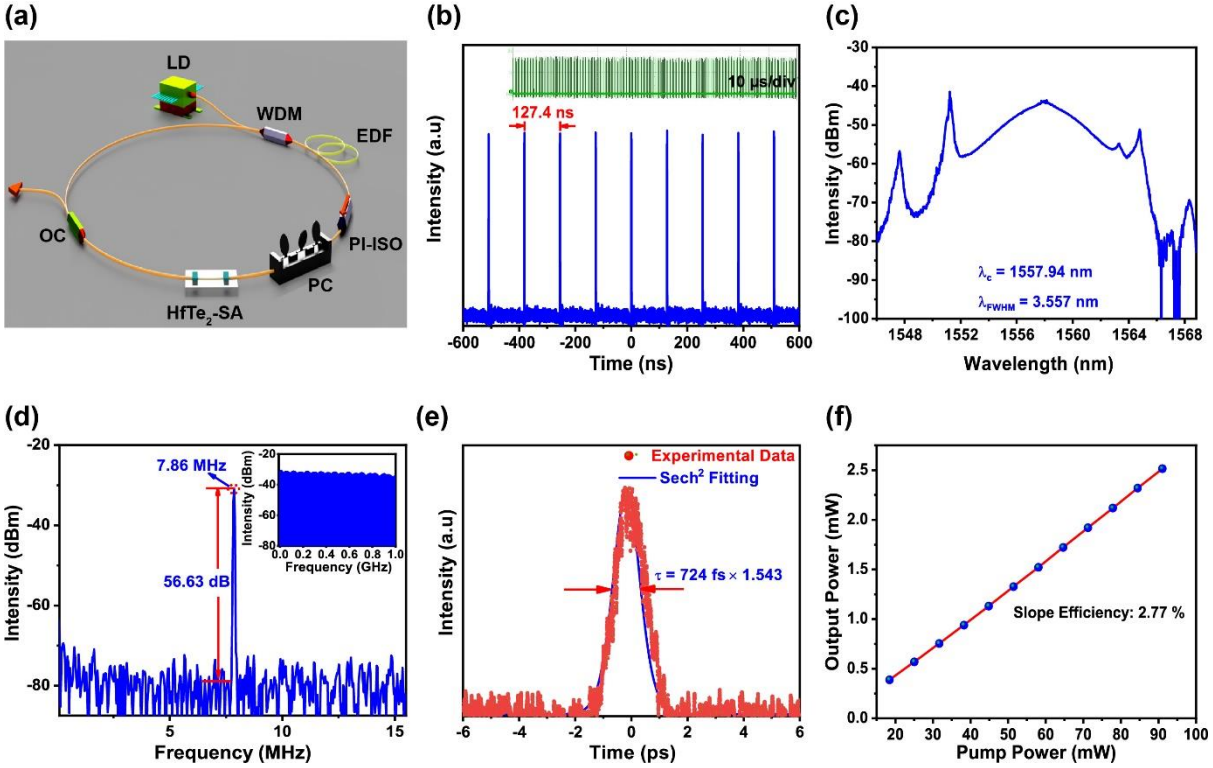

Figure 4. (a) Schematic diagram of all fiber based-ring cavity; The 976 nm laser diode (LD) is used with the gain medium, i.e., Er-doped fiber (EDF); a 10:90 output coupler (OC) is used, where the 90% part was connected with the cavity and 10% with the measuring devices. (b) A pulse train of mode-locked laser; inset is the original oscilloscope image of the long-range pulse train with 10 μs/div. (c) The operational wavelength of the mode-locked laser with a center wavelength of 1557.94 nm and 3-dB bandwidth of 3.557 nm. (d) RF-spectrum with the fundamental frequency of 7.86 MHz. (e) The autocorrelation trace of the mode-locked laser pulse widths with $sech^2$ fitting. (f) Output power corresponds to the input pump power with a slope efficiency of 2.77%. WDM: wavelength division multiplexer; PI-ISO: Polarization-independent isolator; PC: Polarization controller.

Table 2 Comparison of mode-locked lasers based on various 2D-SAs in Er-doped fiber laser cavity.

Material	Incorporation method	λ_c [nm]	Pulse duration	Repetition rate [MHz]/ SNR [dB]	Threshold Pump Power [mW]	Ref.
Graphene	PVA[(a)] composite	1559.1	433 fs	25.67/ 31	**53.30**	[37]
Borophene	Tapered fiber	1560.7	693 fs	16/63	45	[38]
Sb_2Te_3	Fiber end	1558.5	1.9 ps	3.75/ 65	65	[39]
Bi_2Te_3	Tapered fiber	1558.5	1.22 ps	4.88/ -	26.5	[40]
MoS_2	PVA composite	1552	960 fs	12.99/ 55	-	[41]
PtS_2	PVA composite	1572	2.06 ps	15.04/ 43	45.7	[42]
$NbSe_2$-QDs	SPF[(b)]	1556	756 fs	7.7/50	15	[43]
HfS_2	Microfiber	1561.8	221.7 fs	21.45/70	30	[14]
$HfSe_2$	SPF	1561.43	297 fs	18.09/80	28.5	[15]
$MoTe_2$	PVA composite	1557.2	1.1 ps	5.26/-	-	[44]
WTe_2	PVA composite	1556.6	1.15 ps	5.34/-	-	[44]
	PVA composite	1556.2	770 fs	13.94/67	-	[45]
$HfTe_2$	**SPF**	**1557.3**	**724 fs**	**7.86/ 56.63**	**18.35**	**This work**

[(a)] Polyvinyl alcohol
[(b)] Side Polished Fiber

After analyzing the ultrafast laser generation capability of 2D-$HfTe_2$ SA, it is being used to design a single-frequency fiber laser (SFFL) source. SFFLs have a wide range of applications in optical sensing, measurement, and coherent optical communication.[46–48] With the rise of low-dimensional materials, SFFLs based on low-dimensional materials have attracted much attention due to their simpler structures and lower fabrication costs. [31,49] Since there is no report on the single-frequency laser for $HfTe_2$, we built a ring-cavity fiber laser to study it, as shown in Fig. 5(a). An adjustable pump source operating at 980 nm is used in the experiment, and a wavelength division multiplexer feeds the pump light into an erbium-doped gain fiber (EDF, Coherent, 7.2 dB/m, 1.5 m) (WDM), which results in a laser with a 1550 nm wavelength. The circulator's port 2 is connected to an SPF-based $HfTe_2$-SA, a polarization controller (PC), and a fiber Bragg grating with a high reflectivity (99%) in order to produce a single-frequency laser output. A SA absorbs low-power lasers and is bleached by high-

power lasers with saturable absorption effects. When two beams propagating in opposite directions form interference at the SA device, a periodic light intensity distribution is formed here.[50] And it is known from the SA properties that $HfTe_2$ absorbs more for the laser with weaker light intensity and less for the laser with stronger light intensity. Therefore, a periodically shifted refractive index distribution will be formed at SA, forming a transient grating with an extremely narrow bandwidth. By altering the PC, the transient grating's filtering impact can be improved. Because the circulator fixes the direction of laser operation in the cavity, the circulator's port 3 is fused to the coupler (10/90), 90% of the laser is returned to the EDF through the WDM, and 10% of the coupler port is used as the laser output port. In the ultra-narrow lasers, the role of $HfTe_2$ nanosheets is equal to the role of the highly doped gain fiber. Due to the Sagnac effect, it is required to have a SPF-SA in order to adjust the phase of the two-phase transmission beam, such that all incident optical signals can be reflected.[51] Herein, the $HfTe_2$ nanosheets based SPF-SA acts as a transient grating with ultra-narrow linewidth, which has excellent filtering effect.

To monitor the laser's output performance, an oscilloscope (Tektronix MDO3104) and an FP scanning interferometer (SA200-12B, 7.5MHz resolution) were employed. For the duration of the tests, the pump power was set at 350 mW to ensure the laser was operating in single-frequency mode. Fig. 5(b) displays many peaks (blue curve) in one free spectral region before the addition of $HfTe_2$ and shows one peak (red curve) following the addition of SA, demonstrating that the laser was operating at a single frequency at the time.

In order to observe the laser operating state and measure the laser output linewidth, a delayed self-heterodyne system (DSH) was constructed using a frequency spectrum

analyzer (FSA, Rigol DSA 815), a photodetector (PD, EOT-ET5000F), a delayed fiber (100 km), and a 200 MHz acoustic-optical frequency modulator (AOM). The actual outcomes are displayed in Fig. 5(d). Before adding SA, the FSA's sweep width of 0-400 MHz shows many peaks (blue curve), demonstrating that the laser is operating in a multi-longitudinal mode; after adding SA, the number of peaks changes to one (red curve), indicating that the laser is operating in a single-longitudinal mode. The signal obtained after the DSH measurement is a Lorentzian line pattern. The 1/F noise will broaden the line pattern near the center of the self-heterodyne, affecting the experimental accuracy. More accurate experimental results can be obtained by measuring the -20 dB bandwidth of the Lorentz signal.[52] To minimize the possibility of 1/f noise interference, the linewidth was calculated considering the 20 dB. The linewidth measurement results are shown in Fig. 5(e), and the output linewidth of the laser is 1.268kHz.

Then, we described the other characteristics of the laser. Fig. 5(f) illustrates the efficiency of the pump light to signal light conversion. The start-up threshold and slope efficiency of this SFFL are 70 mW and 0.44%, respectively. The highest output power is 2.51 mW at the pump power of 600 mW. However, as the pump power is more than 600 mW, the laser cannot produce a stable single-frequency output. We believe the lower doping concentration of EDF with the higher intracavity insertion loss is the root of the poorer slope efficiency. The findings of the subsequent measurement of the laser's output spectrum using an optical spectrum analyzer (OSA, Yokogawa AQ6370D) are displayed in Fig. 5(c). The operating laser's center wavelength, 1550.34 nm, was in accord with the FBG's center wavelength. At 350 mW of pump power, the laser's signal-to-noise ratio (SNR) was 74.56 dB. Finally, Fig. 5(g) illustrates

the output stability of the SFFL at 400 mW pump power. For one hour, the output power of the SFFL was measured every minute. The standard deviation was 2.97×10^{-2}. Table 3 provides a comparison table of various 2D-SAs for generating SFFLs. The comparison shows that the output linewidth, one of the most important parameters of a single-frequency fiber laser, is inextricably linked to the band gap, size, and concentration of the 2D material and the cavity structure and cavity length of the laser. The achieved linewidth of the SFFL utilizing $HfTe_2$-SA is one of the narrowest of all, and it also has one of the highest SNR and slope efficiency values, as shown in the table. These results suggest that $HfTe_2$-SA is a promising option for ultranarrow photonics applications. To further narrow the linewidth of the SFFL, several future works can be adapted. By utilizing all polarization-maintaining devices, materials with higher absorption, a longer laser cavity, and narrower filters, it is possible to achieve a narrower linewidth of the SFFL.

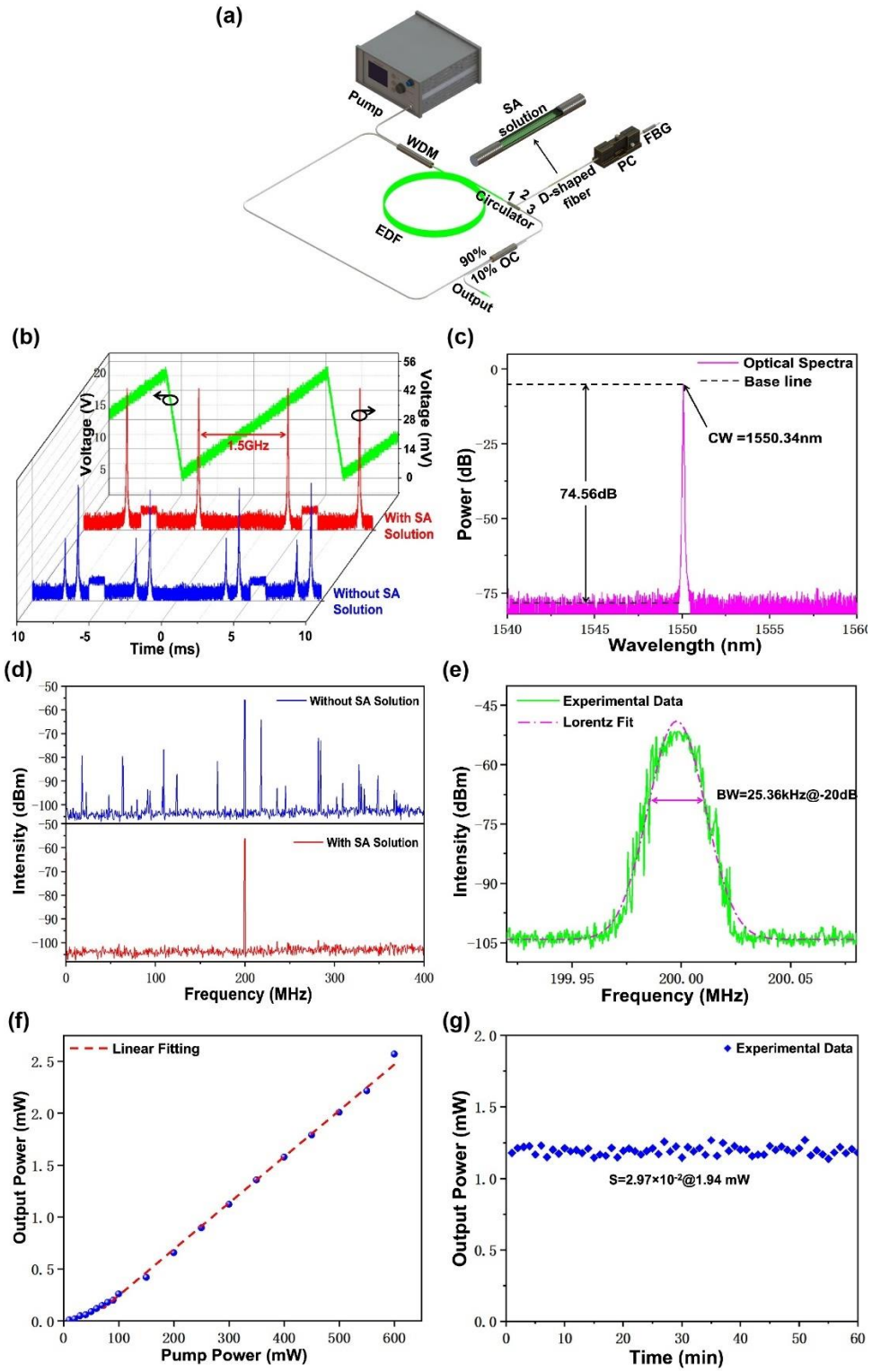

Figure 5. (a) Schematic diagram of the single-frequency fiber laser (SFFL). (b) The variation of the laser signal on an oscilloscope. (c) The optical spectra of SFFL. (d)The variation of the beat signal on the frequency spectrum analyzer. (e) Signal detected by the delayed self-heterodyne system and estimate of the bandwidth (BW) 20 dB down from the maximum. (f) Relationship of the output power versus pump power. (g) Stability of the laser power.

Table 3 Comparison of the output performance of SFFLs based on various 2D materials in Er-doped gain medium. NSs: Nanosheets; QDs: Quantum Dots.

SAs	Slope Efficiency [%]	Linewidth [kHz]	SNR [dB]	Power Fluctuation [%]	Ref.
Graphene	-	206.25	68.3	-	[53]
TI:Bi_2Te_3	-	10	47.5	-	[54]
Ni-MOF	0.19	3.2	52	<1.3	[55]
Ti_2C NSs	0.26	1.3	38	<1.8	[56]
Ti_2C QDs	0.238	1.05	48.99	<0.67	[57]
Ti_3C_2 QDs	1	5	54	<0.75	[31]
Ti_2C@Au NSs	0.207	1	31.82	<0.76	[58]
$GeAs_2$ NSs	-	0.678	80	<2.01	[59]
$HfTe_2$ NSs	**0.44**	**1.268**	**74.56**	**<5.50**	**This Work**

3. Conclusion

In summary, in this work, 2D-HfTe2-nanosheets are prepared using facile liquid phase exfoliation method, and various material characterization are performed to determine the material's thickness, composition, and absorption. The zero bandgap structure of different layers of $HfTe_2$ is realized using the first principal DFT calculation. The prepared nanosheets' excellent and versatile NLO optical properties are determined using open and closed-aperture Z-scan technology. The obtained modulation depth of 11.9 % (800 nm) and 6.35 % (1560 nm), along with transition capability from saturable absorption to reverse saturable absorption, indicates the prepared material's adaptability in nonlinear optics. Finally, $HfTe_2$-based SPF SA is prepared, and the ultrafast and ultranarrow photonics applications are determined. The prepared SA facilitates the generation of a mode-locked laser pulse with a 724 fs pulse width at the second lowest threshold pump power of 18.35 mW for the first time. Additionally, an SFFL is developed with this SA, having one of the narrowest linewidth and highest SNR of 1.268 kHz and 74.56 dB, respectively. These findings indicate that 2D-$HfTe_2$

has great potential in nonlinear optics and can be utilized for further photonic device development.

4. Experimental Section

Material Synthesis

By utilizing the cost-effective and facile liquid phase exfoliation (LPE) method, $HfTe_2$-nanosheets were prepared from the bulk powder. Isopropyl alcohol (IPA) was employed as the solvent due to the low cost and low boiling point. The mixture of IPA and powder was prepared at a rate of 1mg/mL. Then the solution was ultrasonicated for 24 hours at 40 kHz frequency and 400 W output power. To avoid the oxidation of the powder, 28 °C temperature was always maintained by replacing the hot water during ultrasonication. The sample solution was centrifuged (Zonkia HC-3018) at 2000 rpm for 5 min, ensuring no unexfoliated bulk samples were present in the supernatant mixture. The final sample was collected from the supernatant and then spin-coated over quartz substrate and copper grid for further material characterization.

Material Characterization

The prepared nanosheets are characterized by using a scanning electron microscope (SEM, Tescan VEGA3), Raman spectroscopy (WITEC Confocal Raman system, 532 nm laser; 2 mW average power), atomic force microscopy (AFM, Asylum MFP-3D Infinity), XRD (Rigaku SmartLab 9kW - Advance), X-ray photoelectron spectroscopy (XPS, Thermo Fisher Nexsa), field-emission transmission electron microscopy (FETEM, JEOL Model JEM-2100F), and UV-vis-NIR spectrometer (PERKIN ELMER UV-vis-NIR spectrometer).

Z-scan system

The Z-scan analysis was performed with two different laser systems. For 800 nm analysis, a Ti: sapphire laser of 800 nm with 100 femtoseconds (fs) pulse width and 80Hz repetition rate was used. A mode-locked fiber laser with 1 ps pulse durations was used to analyze the result at 1560 nm wavelength. At the center wavelengths of 1560 nm, the laser sources have a repetition rate of roughly 12 MHz. At z = 0, the laser beam was focussed by a plano-convex lens to construct a beam waist (w_0) of approximately 58 µm, determined by a beam profiler (Newport, LBP2-HR-VIS). A drive stage (Thorlabs, DDSM100/M) was utilized to move the sample. Furthermore, the NLO characteristics at 1560 nm were investigated using the photodiode power sensor (Thorlabs, S122C^{h}) and power meter (Thorlabs, PM100D).

Saturable absorber preparation method

In order to ensure that the proper amount of $HfTe_2$ material was deposited over the SPF during the preparation of the SA, the material was carefully dropped onto the SPF. The material solution was initially applied to the SPF three droplets at a time. Additional droplets were added as the material dries. The number of drops was reduced to one when it was determined that the materials were sufficient for obtaining the desired results (through continuous monitoring of the oscilloscope's output). The materials were then dried on the SPF for several minutes. Once the desired result was achieved, the deposition stopped, and the material was allowed to dry overnight at room temperature. The results of the laser pulse operation were acquired after all the materials had dried.

Mode-locked laser performance analysis

The performance of the model-locked laser is characterized by utilizing various equipment, which are an oscilloscope (Teledyne LeCroy: wave pro 804hd), spectrum

analyzer (Yokogawa, AQ6370Bl), photodetectors (Thorlabs, DET01CFC), power meters (Thorlabs, PM20CH), autocorrelator (APE pulse Check SM S08661).

Supporting Information

Supporting Information is available from the Wiley Online Library or from the author.

Conflicts of interest

There is no conflict to declare.

Acknowledgments

S.Ahmed and Y. Gan contributed equally in this paper.

This work is financially supported by the Innovation and Technology Fund, Hong Kong, China (GHP/040/19SZ); National Natural Science Foundation of China (6217030813); Photonic Research Institute, The Hong Kong Polytechnic University (Project number: 1-CD6F and 1-CD6G); the Hong Kong Polytechnic University Shenzhen Research Institute, Shenzhen, China (Grant Code: the science and technology innovation commission of Shenzhen (JCYJ20210324141206017)); Guangdong Basic and Applied Basic Research Foundation (2021A1515010964); Project of Research Institute for Advanced Manufacturing (RIAM) , The Hong Kong Polytechnic University (Project number: 1-CD8V; P0046128); the Science and Technology Innovation Commission of Shenzhen Municipality (SGDX20190919094803949 and JCYJ20200109105810074).

Reference

[1] Y. Huang, Y.-H. Pan, R. Yang, L.-H. Bao, L. Meng, H.-L. Luo, Y.-Q. Cai, G.-D.

Liu, W.-J. Zhao, Z. Zhou, L.-M. Wu, Z.-L. Zhu, M. Huang, L.-W. Liu, L. Liu, P. Cheng, K.-H. Wu, S.-B. Tian, C.-Z. Gu, Y.-G. Shi, Y.-F. Guo, Z. G. Cheng, J.-P. Hu, L. Zhao, G.-H. Yang, E. Sutter, P. Sutter, Y.-L. Wang, W. Ji, X.-J. Zhou, H.-J. Gao, *Nat. Commun. 2020 111* **2020**, *11*, 1.

[2] H. Long, Y. Shi, Q. Wen, Y. H. Tsang, *J. Mater. Chem. C* **2019**, *7*, 5937.

[3] L. Wang, L. Huang, W. C. Tan, X. Feng, L. Chen, X. Huang, K.-W. Ang, *Small Methods* **2018**, *2*, 1700294.

[4] Z. Wei, B. Li, C. Xia, Y. Cui, J. He, J.-B. Xia, J. Li, *Small Methods* **2018**, *2*, 1800094.

[5] L. Gao, H. Chen, F. Zhang, S. Mei, Y. Zhang, W. Bao, C. Ma, P. Yin, J. Guo, X. Jiang, S. Xu, W. Huang, X. Feng, F. Xu, S. Wei, H. Zhang, *Small Methods* **2020**, *4*, 2000250.

[6] P. C. Debnath, K. Park, Y.-W. Song, *Small Methods* **2018**, *2*, 1700315.

[7] Y. Yi, Z. Sun, J. Li, P. K. Chu, X. Yu, *Small Methods* **2019**, *3*, 1900165.

[8] W. Gao, L. Huang, J. Xu, Y. Chen, C. Zhu, Z. Nie, Y. Li, X. Wang, Z. Xie, S. Zhu, J. Xu, X. Wan, C. Zhang, Y. Xu, Y. Shi, F. Wang, *Appl. Phys. Lett.* **2018**, *112*, 171112.

[9] W. Yu, Z. Dong, I. Abdelwahab, X. Zhao, J. Shi, Y. Shao, J. Li, X. Hu, R. Li, T. Ma, Z. Wang, Q.-H. Xu, D. Y. Tang, Y. Song, K. P. Loh, *ACS Nano* **2021**, *15*, 18448.

[10] M. L. Adam, A. A. Bala, *Comput. Condens. Matter* **2021**, *26*, e00527.

[11] D. Chakraborty, P. Johari, *ACS Appl. Nano Mater.* **2020**, *3*, 5160.

[12] A. M. Saleque, S. Ahmed, M. N. A. S. Ivan, M. I. Hossain, W. Qarony, P. K. Cheng, J. Qiao, Z. L. Guo, L. Zeng, Y. H. Tsang, *Nano Energy* **2022**, *94*, 106916.

[13] Y. Li, H. Chen, Y. Guo, K. Wang, Y. Zhang, P. Lan, J. Guo, W. Zhang, H. Zhong,

Z. Guo, Z. Zhuang, Z. Liu, *Photonics Res.* **2021**, *9*, 1039.

[14] J. Yin, F. Zhu, J. Lai, H. Chen, M. Zhang, J. Zhang, J. Wang, T. He, B. Zhang, J. Yuan, P. Yan, S. Ruan, *Adv. Opt. Mater.* **2019**, *7*, 1801303.

[15] X. Wu, Z. Zhou, J. Yin, M. Zhang, L. Zhou, Q. Na, J. Wang, Y. Yu, J. Wang, R. Chi, P. Yan, *Nanotechnology* **2020**, *31*, 245204.

[16] D. Hodul, M. J. Sienko, *Phys. B+C* **1980**, *99*, 215.

[17] L.-X. Zhao, X.-C. Huang, al -, K. Jia, C.-L. Yang, M.-S. Wang, S. Aminalragia-Giamini, J. Marquez-Velasco, P. Tsipas, D. Tsoutsou, G. Renaud, A. Dimoulas, *2D Mater.* **2016**, *4*, 015001.

[18] P. C. Klipstein, D. R. P. Guy, E. A. Marseglia, J. I. Meakin, R. H. Friend, A. D. Yoffe, *J. Phys. C Solid State Phys.* **1986**, *19*, 4953.

[19] Y. Nakata, K. Sugawara, A. Chainani, K. Yamauchi, K. Nakayama, S. Souma, P.-Y. Chuang, C.-M. Cheng, T. Oguchi, K. Ueno, T. Takahashi, T. Sato, *Phys. Rev. Mater.* **2019**, *3*, 071001.

[20] Z. Peng, X. Chen, Y. Fan, D. J. Srolovitz, D. Lei, *Light Sci. Appl. 2020 91* **2020**, *9*, 1.

[21] S. Mangelsen, P. G. Naumov, O. I. Barkalov, S. A. Medvedev, W. Schnelle, M. Bobnar, S. Mankovsky, S. Polesya, C. Näther, H. Ebert, W. Bensch, *Phys. Rev. B* **2017**, *96*, 1.

[22] Z. Sun, X. Jiang, Q. Wen, W. Li, H. Zhang, *J. Mater. Chem. C* **2019**, *7*, 4662.

[23] Y. Gan, F. Zhu, Y. Shi, Q. Wen, *J. Mater. Chem. C* **2021**, *9*, 2276.

[24] C. Y. Xu, P. X. Zhang, L. Yan, *J. Raman Spectrosc.* **2001**, *32*, 862.

[25] S. Ahmed, P. K. Cheng, J. Qiao, W. Gao, A. M. Saleque, M. N. Al Subri Ivan, T. Wang, T. I. Alam, S. U. Hani, Z. L. Guo, S. F. Yu, Y. H. Tsang, *ACS Nano* **2022**, *16*, 12390.

[26] S. Ahmed, J. Qiao, P. K. Cheng, A. M. Saleque, M. N. A. S. Ivan, T. I. Alam, Y. H. Tsang, *ACS Appl. Mater. Interfaces* **2021**, *13*, 61518.

[27] G. Kresse, D. Joubert, *Phys. Rev. B* **1999**, *59*, 1758.

[28] J. P. Perdew, K. Burke, M. Ernzerhof, *Phys. Rev. Lett.* **1996**, *77*, 3865.

[29] F. Bonaccorso, Z. Sun, T. Hasan, A. C. Ferrari, *Nat. Photonics* **2010**, *4*, 611.

[30] W.-Y. Kong, G.-A. Wu, K.-Y. Wang, T.-F. Zhang, Y.-F. Zou, D.-D. Wang, L.-B. Luo, *Adv. Mater.* **2016**, *28*, 10725.

[31] N. Xu, H. Li, Y. Gan, H. Chen, W. Li, F. Zhang, X. Jiang, Y. Shi, J. Liu, Q. Wen, H. Zhang, *Adv. Sci.* **2020**, *7*, 2002209.

[32] C. Ye, Z. Yang, J. Dong, Y. Huang, M. Song, B. Sa, J. Zheng, H. Zhan, *Small* **2021**, *17*, 2103938.

[33] J. K. Zaręba, M. Nyk, M. Samoć, *Adv. Opt. Mater.* **2021**, *9*, 2100216.

[34] J. Wang, Y. Chen, R. Li, H. Dong, Y. Ju, J. He, J. Fan, K. Wang, K. S. Liao, L. Zhang, S. A. Curran, W. J. Blau, *J. Inorg. Organomet. Polym. Mater.* **2011**, *21*, 736.

[35] S. Liu, M. Wang, S. Yin, Z. Xie, Z. Wang, S. Zhou, P. Chen, *Phys. status solidi* **2019**, *216*, 1800837.

[36] P. K. Cheng, S. Ahmed, J. Qiao, L. W. Wong, C. F. Yuen, A. M. Saleque, M. N. A. S. Ivan, S. U. Hani, M. I. Hossain, J. Zhao, Q. Wen, Y. H. Tsang, *Appl. Mater. Today* **2022**, *26*, 101296.

[37] P. L. Huang, S.-C. Lin, C.-Y. Yeh, H.-H. Kuo, S.-H. Huang, G.-R. Lin, L.-J. Li, C.-Y. Su, W.-H. Cheng, *Opt. Express* **2012**, *20*, 2460.

[38] J. S. Liu, X. H. Li, Y. X. Guo, A. Qyyum, Z. J. Shi, T. C. Feng, Y. Zhang, C. X. Jiang, X. F. Liu, *Small* **2019**, *15*, 1902811.

[39] J. Sotor, G. Sobon, W. Macherzynski, K. M. Abramski, *Laser Phys. Lett.* **2014**,

11, 055102.

[40] Z.-C. Luo, M. Liu, H. Liu, X.-W. Zheng, A.-P. Luo, C.-J. Zhao, H. Zhang, S.-C. Wen, W.-C. Xu, *Opt. Lett.* **2013**, *38*, 5212.

[41] M. Zhang, R. C. T. Howe, R. I. Woodward, E. J. R. Kelleher, F. Torrisi, G. Hu, S. V Popov, J. R. Taylor, T. Hasan, *Nano Res.* **2015**, *8*, 1522.

[42] H. Long, C. Y. Tang, P. K. Cheng, X. Y. Wang, W. Qarony, Y. H. Tsang, *J. Light. Technol.* **2019**, *37*, 1174.

[43] L. Li, L. Pang, Q. Zhao, Y. Wang, W. Liu, *Nanoscale* **2020**, *12*, 4537.

[44] D. Mao, B. Du, D. Yang, S. Zhang, Y. Wang, W. Zhang, X. She, H. Cheng, H. Zeng, J. Zhao, *Small* **2016**, *12*, 1489.

[45] J. Koo, Y. I. Jhon, J. Park, J. Lee, Y. M. Jhon, J. H. Lee, *Adv. Funct. Mater.* **2016**, *26*, 7454.

[46] D. Pan, C. Ke, S. Fu, Y. Liu, D. Liu, A. E. Willner, *Opt. Lett.* **2013**, *38*, 5220.

[47] F. Yang, Q. Ye, Z. Pan, D. Chen, H. Cai, R. Qu, Z. Yang, Q. Zhang, *Opt. Commun.* **2012**, *285*, 149.

[48] S. Diaz, S. Abad, M. Lopez-Amo, *Laser Photon. Rev.* **2008**, *2*, 480.

[49] Z. Feng, G. Yiyu, J. Libin, W. Qiao, *Laser Photon. Rev.* **2021**, *15*, 2100059.

[50] H.-C. Chien, C.-H. Yeh, C.-C. Lee, S. Chi, *Opt. Commun.* **2005**, *250*, 163.

[51] S. A. Havstad, B. Fischer, A. E. Willner, M. G. Wickham, *Opt. Lett.* **1999**, *24*, 1466

[52] L. B. Mercer, *J. Light. Technol.* **1991**, *9*, 485.

[53] F. D. Muhammad, M. Z. Zulkifli, A. A. Latif, S. W. Harun, H. Ahmad, *IEEE Photonics J.* **2012**, *4*, 467.

[54] H. Zhang, S. Chen, Y. Li, S. Wen, Q. Wang, C. Zhao, *J. Light. Technol. Vol. 32, Issue 22, pp. 3836-3842* **2014**, *32*, 3836.

[55] Z. Sun, X. Jiang, Q. Wen, W. Li, H. Zhang, *J. Mater. Chem. C* **2019**, *7*, 4662.

[56] Y. Gan, F. Zhu, Y. Shi, Q. Wen, *J. Mater. Chem. C* **2021**, *9*, 2276.

[57] X. Liu, L. Ji, F. Zhu, Y. Gan, Q. Wen, *Opt. Mater.* **2021**, *122*, 111686.

[58] Y. Wang, S. Liu, F. Zhu, Y. Gan, Q. Wen, *Nanomaterials* **2021**, *11*, 1995.

[59] S. Liu, G. Li, F. Zhu, H. Huang, J. Lu, J. Qu, L. Li, Q. Wen, *Adv. Funct. Mater.* **2022**, *32*, 2112252.

Table of Content

Herein, the potential application of 2D-$HfTe_2$ nanosheets in nonlinear optics and photonics are discussed. A mode-locked laser with 724 fs pulsed width is realized using a side-polished fiber-based $HfTe_2$-saturable absorber, at a second-lowest mode-locking threshold pump power among 2D material-based SAs. Finally, the $HfTe_2$-SA is used to generate a highly stable single-frequency fiber laser illuistrating its promising ultranarrow photonic applications.

Safayet Ahmed[1,3,†], Yiyu Gan[2,†], Ahmed Mortuza Saleque [1,3], Honglei Wu[2], Junpeng Qiao[4], Md. Nahian Al Subri Ivan[1,3], Sumaiya Umme Hani[1,3], Tawsif Ibne Alam[1,3], Qiao Wen[2*] and Yuen Hong Tsang[1,3*]

2D Semi-metallic Hafnium Ditelluride: A Novel Nonlinear Optical Material for Ultrafast and Ultranarrow Photonics Applications